Health Monitoring of UAV Wing Skin-to-spar Joints Using Guided Waves and Macro Fiber Composite Transducers

Francesco Lanza di Scalea[1,*], Howard Matt[1], Ivan Bartoli[1], Stefano Coccia[1], Gyuhae Park[2], Charles Farrar[2]

[1]*NDE & Structural Health Monitoring Laboratory*
Department of Structural Engineering, University of California, San Diego
9500 Gilman Drive, M.C. 0085, La Jolla, California 92093-0085, USA

[2]*Engineering Sciences & Applications, Engineering Institute, MS T001*
Los Alamos National Laboratory
Los Alamos, NM 87545, USA

[*]corresponding author: (858) 822-1458, Fax: (858) 534-6373, E-mail: flanza@ucsd.edu

Keywords: Unmanned Aerial Vehicles, ultrasonic guided waves, Macro Fiber Composites, Discrete Wavelet Transform, structural health monitoring

ABSTRACT

This paper deals with the monitoring of the composite wing skin-to-spar joint in Unmanned Aerial Vehicles using ultrasonic guided waves. The study investigates simulated wing skin-to-spar joints with two different types of bond defects, namely poorly-cured adhesive and disbonded interfaces. The bond-sensitive feature considered is the ultrasonic strength of transmission through the joints. The dispersive wave propagation problem is studied numerically by a semi-analytical finite element method that accounts for viscoelastic damping, and experimentally by ultrasonic testing that uses highly durable, flexible Macro Fiber Composite transducers. The Discrete Wavelet Transform is also employed to de-noise and compress the ultrasonic measurements. Both the numerical and the experimental tests confirm that the ultrasonic strength of transmission increases across the defected bonds.

INTRODUCTION

Fiber-reinforced polymer composites are being increasingly utilized in the aerospace industry due to their light weight and high strength characteristics. One example of a heavy use of composites is found in Unmanned Aerial Vehicles (UAV's) which are employed for both military and civil purposes. Adhesively-bonded joints are found in the wing skin-to-spar assemblies of UAVs. These joints are critical structural components, necessitating of effective tools for assessing their condition. To monitor in-flight damage and reduce life-cycle costs of the aircraft, a continuous built-in structural health monitoring approach, rather than a traditional NDT-type maintenance approach, would be most desirable.

Ultrasonic guided waves, propagating in structural components with finite cross-sectional dimensions such as aerospace skin panels, lend themselves for built-in structural monitoring systems. Guided waves can afford long ranges as well as large sensitivity to damage due to the virtually endless mode-frequency combinations. Several guided wave features, including amplitude, velocity and frequencies, have been shown to be sensitive to the properties of adhesive layers, particularly the adhesive longitudinal stiffness, shear stiffness, as well as its thickness which, in turn, is related to strength. In some of these studies the guided waves were both generated and detected within the bonded region (Nagy and Adler, 1989; Mal, Xu, and Bar-Cohen, 1990; Lowe and Cawley, 1994; Kundu et al., 1998; Rose, Zhu, and Zaidi, 1998; Heller, Jacobs, and Qu, 2000; Seifried, Jacobs, and Qu, 2002; Hay et al., 2003). In other instances, the waves were generated in the adherend on one side of the bond and received across the bond (Rose, Rajana, and Hansch, 1995; Chang and Mal, 1995; Mal, Chang, and Guo, 1996; Lowe, Challis, and Chan, 2000; Lanza di Scalea, Bonomo, and Tuzzeo, 2001; Sun, Rose, and Zaidi, 2002; Lanza di Scalea, Rizzo, and Marzani, 2004). The "across the bond" testing configuration is particularly successful for the inspection of lap-shear joints, tear strap-to-skin joints, and bonded patch repairs for damaged aircraft panels. The advantage of this approach is the ability to cover the entire width of the bonded overlap.

These previous studies provided a great deal of knowledge on the behavior and the defect sensitivity of various guided wave modes propagating in adhesively-bonded joints. However, none of these works examined the case of composite-to-composite bonded joints, such as those found in the wing skin-to-spar connections of UAVs. In addition, previous works on guided

wave inspection of bonds were not focused on built-in structural monitoring systems since they used traditional wedge-based, water-coupled or non-contact ultrasonic transduction.

As further advances are made in the field of structural health monitoring based on guided waves, the transition from lab environment to the field will require the use of reliable, highly-robust and, possibly, flexible transducers as opposed to the traditional monolithic and brittle $Pb(Zr\text{-}Ti)O_3$ - PZT transducers. In response to this demand, piezoelectric films (poly(vinylidene fluoride)) - PVDFs have been proposed for guided wave transduction (Monkhouse, Wilcox, and Cawley, 1997; Gu, Lloyd, and Wang, 2005). Although PVDF transducers bring the advantages of durability and flexibility when compared to PZT transducers, their reduced electro-mechanical coupling efficiency requires increased actuation power in generation and heavy amplification in detection. The fact that PVDFs work best in the high-frequency range (500 kHz – 4 MHz) poses some limitations in terms of increased wave attenuation. Finally, the large temperature dependency of the PVDF coupling efficiency is another aspect of concern.

Other transducers are being developed in an effort to couple the electro-mechanical efficiency of PZTs with the flexibility of PVDFs. These include the Active Fiber Composites - AFCs and the Macro Fiber Composites - MFCs type P1 developed at NASA Langley Research Center. Both transducers are made of very thin, piezoceramic fibers that are unidirectionally aligned and sandwiched between two sets of inter-digitated electrodes (Williams and Inman, 2002). This electrode arrangement provides an electric field that exploits the large, in-plane (3-3) electro-mechanical coupling (Wilkie et al., 2000). AFC transducers have been used for guided wave transduction in the low hundreds of kHz range (Barbezat et al., 2004; Brunner et al. 2004). MFC transducers have been primarily utilized for structural control and vibration suppression (Wilkie et al. 2000; Bevan and Mei, 2001; Schonecker et al., 2005), and, in one case, as guided wave transducers for pipe inspections (Thien et al., 2005). The main advantage of MFCs over AFCs is the reduced manufacturing cost. The circular AFC fibers are manufactured through a very costly extrusion process, as opposed to the rectangular fibers of MFCs which are cut from monolithic piezoceramic wafers.

In the present study, MFC transducers were used to generate and detect ultrasonic guided waves across composite-to-composite joints that simulated the wing skin-to-spar connection of UAVs. This work is part of a broader effort aimed at developing an on-board structural health monitoring system for UAV wings. It is demonstrated that bond defects, including poorly-cured

adhesive and disbonds, result in an increased strength of transmission of the s_0 mode that is generated and detected by the MFC transducers. It is further demonstrated that the application of the Discrete Wavelet Transform to the detected ultrasonic signals can be highly beneficial for de-noising and compression purposes. The experimental results are preceded by a semi-analytical finite element model that predicts the complete dispersive behavior of the waves propagating in the skin-to-spar joints, accounting for material viscoelastic damping. The model corroborates the experimental finding of increased ultrasonic strength of transmission across the defected bonds.

PROBLEM STATEMENT

A partial cross-section of a typical UAV wing assembly is shown in Figure 1(a). The wing skin is generally made of a Nomex or aluminum honeycomb core sandwiched between two carbon fiber-reinforced plastic (CFRP) laminated composite plates. Each skin is bonded using high strength epoxy adhesive to a tubular CFRP spar that runs down the length of the wing. The sandwiched skin tapers down in the bonded region, where only the CFRP laminates are bonded to the spar. The theoretical and experimental tests that follow were performed on two composite plates directly bonded to the spar. These systems are a sufficiently accurate representation of the wing skin-to-spar joint when the ultrasonic transducers are installed in close proximity to the bonded region.

The different bond conditions that were examined included regions with poorly-cured adhesive and disbonded regions, in addition to regions with properly-cured adhesive. The poorly-cured adhesive was obtained by mixing an improper epoxy-hardener ratio that resulted in an approximate 50% degradation in longitudinal and shear stiffness compared to the properly-cured values. Two disbonded regions of different size were created by inserting Teflon release films with a thickness of 0.025 mm at the bondline. The release film was expected to severly degrade the shear stiffness of the bond while degrading its longitudinal stiffness to a smaller extent. The two simulated disbonds had dimensions of 12.7 mm × 12.7 mm and 25.4 mm × 25.4 mm, respectively. The total bond thickess was measured to be 0.203 mm.

Two different plate lay-ups were studied for the skin, namely a quasi-isotropic $[0/\pm45/90]_S$ lay-up and a $[0/\pm45/0]_S$ lay-up, both consisting of eight T700/5208 CFRP plies and having overall dimensions of 330 mm × 330 mm × 1.067 mm. The $[0/\pm45/0]_S$ lay-up is most commonly used in UAVs, where the 0-deg fibers and ±45-deg fibers provide flexural and torsional rigidity,

respectively, to the wing. The quasi-isotropic lay-up was examined as a simplified model of the UAV wing. The two plates were bonded to woven [0/90] T800/924 CFRP square tubes with outer dimensions of 50.8 mm × 50.8 mm and a wall thickness of 5.23 mm. Bonding of the plates was done such that the 0-deg fiber direction of the plates ran along the lengthwise direction of the spar.

Analyses and experiments were performed in the "across the bond" test configuration, depicted in Figure 1(b), whereby guided waves were generated and detected by a pair of MFC transducers located in the skin across the joint. The different states of the bond were discriminated by monitoring the changes in ultrasonic strength of transmission across the joint, as determined by features extracted from the time domain signals and the corresponding wavelet coefficients. Pictures of one of the simulated wing skin-to-spar joints, showing the bond defects and the MFC actuator/sensor pair, are shown in Figures 1(c) and 1(d).

GUIDED WAVE MODELING

Modeling Formulation and Procedure

Modal solutions for the dispersive waves were obtained by a Semi-Analytical Finite Element (SAFE) approach. The SAFE technique requires only the discretization of the cross-section of the waveguide, thus reducing a 3-D problem to a 2-D one. Harmonic behavior of the displacements is then imposed in the wave propagation direction, and the dispersive solutions are obtained from an eigenvalue problem. Because of their computational efficiency, SAFE methods have been utilized in the past to study waves propagating in waveguides of arbitrary cross-sections (Gavrić, 1995; Hayashi, Song, and Rose, 2003; Finnveden, 2004), including FRP laminates (Mukdadi et al., 2002; Mukdadi and Datta, 2003). The novelty of the SAFE method used in the present work is the introduction of viscoelastic material damping for both the CFRP adherends and the adhesive layer. Material damping is accounted for by allowing the constitutive stiffness matrices to be complex.

SAFE models were created for the wing skin and for the skin-to-spar bonded region, respectively, as illustrated by the dashed lines in Figure 2(a). The energy transmission through the joint is controlled by the "carrier modes" propagating in the bonded region that are excited by the s_0 mode generated by the MFC actuator in the wing skin. These carrier modes are created by mode conversion effects at the bond edges. In turn, the mode conversion depends on the similarity between cross-sectional displacement mode shapes. The same argument was used in

previous works dealing with guided wave inspection of aluminum lap-shear joints (Lowe, Challis, and Chan, 2000; Lanza di Scalea, Rizzo, and Marzani, 2004).

The model assumed a uniform thickness for the spar, neglecting the localized increase in thickness at the bond edges due to the spar tubular geometry. This approximation was considered acceptable since the frequency content of the waves examined was such that their penetration beyond the wall thickness of the spar was negligible.

The SAFE method was implemented in Matlab© using the Partial Differential Equation toolbox for creating the finite element mesh. The waveguide was modeled as a system of N homogeneous and viscoelastic anisotropic layers. As shown in Figure 2(b), the dimensions were considered infinite in the width direction, y, perpendicular to the wave propagation direction, x. Thus the wave propagation problem could be studied by simply considering a longitudinal section in the x-z wave propagation plane. The section was discretized in the thickness direction, z, by a set of one-dimensional finite elements with quadratic shape functions and three nodes, with three degrees of freedom per node as shown in Figure 2(b). Details on the general SAFE procedures followed to extract the dispersive solutions, in terms of phase velocity, energy velocity, attenuation curves and cross-sectional mode shapes, were discussed by Bartoli et al. (2005).

In summary, the eigenproblem solutions are obtained in terms of complex wavenumbers $k = k_{real} + j\ k_{im}$ (j is the imaginary unit) and corresponding frequencies ω. The real part of the wavenumber is used to evaluate the phase velocity as $c_{ph}=\omega/k_{real}$. The imaginary part of the wavenumber corresponds to the frequency-dependent attenuation, in Nepers per meter.

The energy velocity, rather than the conventional group velocity $\partial\omega/\partial k$, was used as the only physically meaningful parameter for viscoelastic media (Bernard, Lowe, and Deschamps, 2001). The expression for the energy velocity used in the present work is:

$$V_e = \frac{\frac{1}{H}\int_H \mathbf{P}\cdot\hat{\mathbf{x}}dz}{\frac{1}{T}\int_T\left(\frac{1}{H}\int_H Edz\right)dt} \qquad (1)$$

where $\hat{\mathbf{x}}$ is the vector of unit length along the wave propagation direction, x, H is the entire waveguide thickness, and $1/T\int_T(..)dt$ denotes the average over the time period, T. The integral $1/H\int_H(..)dz$ evaluates the average power computed from the Poynting vector, $\mathbf{P}$ (real part only) and the average total energy density (kinetic and potential), E, over the waveguide thickness. The Poynting vector can be calculated from the known relation:

$$\mathbf{P} = -\frac{1}{2}\mathrm{Re}(\boldsymbol{\sigma}\dot{\mathbf{u}}^{*}) = \begin{pmatrix} P_x \\ P_y \\ P_z \end{pmatrix} \tag{2}$$

where $\boldsymbol{\sigma}$ is the classical 3×3 stress tensor and $\dot{\mathbf{u}}^{*}$ is the complex conjugate of the particle velocity vector. The P_x component of the Poynting vector, which represents the power flow in the direction of wave propagation carried by a particular mode, was used to predict the wave transmission strength across the different bond conditions.

Complex stiffness matrices, $\mathbf{C}^{*}$, were used in the governing eigenvalue problem to represent viscoelastic material damping in all components of the skin-to-spar joint models. The Hysteretic viscoelastic model was assumed, where the imaginary part of the stiffness matrix is independent of frequency, following:

$$C_{ij}^{*} = C_{ij}^{'} - j\,C_{ij}^{''} \tag{3}$$

The values of the real components, $C_{ij}^{'}$, and of the imaginary components, $C_{ij}^{''}$, of the stiffness matrices adopted in the models in the principal directions of material symmetry are shown in Table 1.

For the eight CFRP laminae of the skin, the real components of the stiffness matrix were based upon manufacturing specifications and typical values for T300/5208 carbon epoxy. The imaginary components of the stiffness matrix were derived from the values used by Neau, Lowe and Deschamps (2002). The stiffness matrix of each lamina was opportunely rotated before the finite element assembly step. In particular, if the wave propagation direction, *x*, was oriented at an angle θ with respect to a lamina's fiber direction, *1*, the stiffness matrix for that lamina was calculated as:

$$\mathbf{C}_{\theta}^{*} = \mathbf{R}_1\,\mathbf{C}^{*}\mathbf{R}_2^{-1} \tag{4}$$

where $\mathbf{C}^{*}$ is the stiffness matrix in the lamina's principal directions, and $\mathbf{R}_1$ and $\mathbf{R}_2$ are the rotation matrices:

$$\mathbf{R}_1 = \begin{bmatrix} m^2 & n^2 & 0 & 0 & 0 & 2mn \\ n^2 & m^2 & 0 & 0 & 0 & -2mn \\ 0 & 0 & 1 & 0 & 0 & 0 \\ 0 & 0 & 0 & m & -n & 0 \\ 0 & 0 & 0 & n & m & 0 \\ -mn & mn & 0 & 0 & 0 & m^2 - n^2 \end{bmatrix}, \quad \mathbf{R}_2 = \begin{bmatrix} m^2 & n^2 & 0 & 0 & 0 & mn \\ n^2 & m^2 & 0 & 0 & 0 & -mn \\ 0 & 0 & 1 & 0 & 0 & 0 \\ 0 & 0 & 0 & m & -n & 0 \\ 0 & 0 & 0 & n & m & 0 \\ -2mn & 2mn & 0 & 0 & 0 & m^2 - n^2 \end{bmatrix} \tag{5}$$

with m=cosθ and n=sinθ.

The CFRP spar was modeled as one homogenous layer with anisotropic properties equivalent to the multilayer [0/90] structure of T800/924, where the complex constitutive matrix was computed by averaging both the real and imaginary coefficients of the global stiffness matrices of two adjacent layers.

The epoxy adhesive was modeled as a viscoelastic isotropic layer. In this case the viscoelastic matrix depends only on the two elastic constants, Young's modulus, E, and shear modulus, G. These constants were calculated from the bulk longitudinal and shear wave velocities, c_L^* and c_S^*. These velocities, that are complex because of the viscoelastic behavior, were in turn calculated by the expression:

$$c_{L,S}^* = c_{L,S}\left(1 + j\frac{\alpha_{L,S}}{2\pi}\right)^{-1} \tag{6}$$

where $\alpha_{L,S}$ are the longitudinal and shear attenuation in the material, expressed in Nepers per wavelength, and $c_{L,S}$ are the experimentally-determined bulk velocities. The attenuation and elastic constants for the properly-cured epoxy and for the poorly-cured epoxy were obtained from normal-incidence ultrasonic tests on properly-mixed and poorly-mixed bulk epoxy samples. The poorly-cured epoxy resulted in a 42% degradation of the Young's modulus and a 44% degradation of the shear modulus compared to the properly-cured epoxy.

Disbonds were simulated in the model by reducing the shear wave velocity (real part) of the properly-cured adhesive by a factor of 100, reducing the longitudinal wave velocity by a factor of 10, and increasing the longitudinal and shear attenuation by a factor of 10. The dramatic degradation in shear velocity was aimed at reflecting the inability of the disbond to transfer shear stresses due to the negligible shear stiffness. The properties assumed for the various bond conditions are summarized in Table 1 in terms of stiffness coefficients, and in Table 2 in terms of bulk ultrasonic velocities and attenuations.

Convergence of the dispersion solutions was found satisfactory using one element for each lamina in the wing skin, one element for the bond layer, and five elements for the spar.

Dispersion Results for Different Bond States

Phase velocity, energy velocity and attenuation curves were obtained from the SAFE models for the three bond conditions examined (properly-cured bond, poorly-cured bond and disbonded interface), considering both wing skin lay-ups ($[0/\pm45/90]_S$ and $[0/\pm45/0]_S$) and wave propagation across the joint.

For the ease of the reader, throughout this paper the conventional nomenclature of symmetric or antisymmetric character is used for all guided modes. However, the only true symmetric and antisymmetric modes exist when considering just the wing skin plate. The modes in the skin-to-spar bond are not truly symmetric nor antisymmetric because the cross-section is not symmetric about its mid-plane. These modes with be indicated with an upper case. Due to the presence of the ±45 deg plies, the horizontally and vertically polarized partial waves are generally not de-coupled, and thus the dispersion curves presented always include both Lamb and shear horizontal modes. For the sake of brevity, dispersion results will be shown here only for the $[0/\pm45/0]_S$ lay-up.

The results for the [0/±45/0]s plate bonded to the spar with the properly-cured adhesive are presented in Figure 3 in the DC-300 kHz range that included the operating range of the experimental tests. The four modes of interest here are the zero-order symmetric, S_0, the zero- and first-order antisymmetric, A_0 and A_1, and the zero-order shear horizontal, SH_0. Figures 3(b) and 3(c) show that A_1 is propagative only above 135 kHz, whereas the other three modes are propagative throughout the entire frequency range considered. Although other higher-order modes exist with cut-on frequencies above 135 kHz, Figure 3(b), they are not considered further due to their large attenuation, Figure 3(c).

Modes S_0 and A_1 have overall minimum attenuation (S_0 below 200 kHz and A_1 above 200 kHz, respectively). Also, their cross-sectional strain profiles, shown in Figure 3(d) at 205 kHz, indicate that both modes produce a concentration of normal strain, ε_{zz}, and shear strain, γ_{xz}, within the adhesive layer. Consequently, they are preferred candidates for monitoring changes in the longitudinal and the shear stiffness of the adhesive. Between the two modes, it is S_0 that

produces the larger concentration of strain at the bondline, suggesting a larger sensitivity to bond state.

Further examination of Figure 3 reveals a mode coupling effect occurring for both S_0 and A_1 between 180 kHz and 220 kHz, that is due to viscoelastic damping and multilayer geometrical effects. Mode coupling is generally associated to sharp changes in energy velocity, increased attenuation, and large transfer of energy across the thickness of the waveguide (Bernard, Lowe, and Deschamps, 2001). The first two phenomena are clearly visible in Figures 3(b) and 3(c) for both S_0 and A_1. The third phenomenon is particularly relevant for the bond monitoring system proposed here, that is based on relating bond defects to an increased strength of transmission through the joint. Exciting modes with large energy transfer between adherends, such as S_0 and A_1 at mode coupling frequencies, would clearly be beneficial in this case. This observation will be confirmed by the experimental tests that follow.

The dispersion curves for the case of the poorly-cured bond, where only the material properties within the thin bond layer were altered according to Table 1, did not show any notable change from those of the properly-cured bond shown in Figure 3. This is because the thickness of the bond layer was very small compared to the thickness of the entire skin-to-spar assembly that dominates the wave dispersive behavior. However, substantial changes in the wave power flow between the two cases were predicted, as discussed in the following sections.

As for the disbond case, shown in Figure 4, substantial changes in the phase velocity, energy velocity and attenuation curves are evident compared to the properly-bonded joint. The main novelty is the appearance of additional modes that did not exist for either of the two bond cases discussed previously. Two separate types of modes propagate in a disbonded joint, namely those whose energy is mainly concentrated within the upper plate above the bondline (identified in Figure 4 by $S_{0,plate}$, $A_{0,plate}$, $SH_{0,plate}$, etc.), and those whose energy is mainly concentrated within the spar below the bondline (identified by $S_{0,spar}$, $A_{0,spar}$, $SH_{0,spar}$, etc.). The "plate" modes in the disbonded joint essentially follow the solutions that would be obtained if the wing-skin plate were analyzed alone, identified in the figure with a lower case (s_0, a_0, sh_0) and represented by the open dots. Under the testing conditions used in this study, the predominant carrier of energy through the disbonded joint is $S_{0,plate}$, that should thus be considered the most relevant mode in Figure 4.

Carrier Modes

Mode conversion occurs at the bond edges due to the transition of wave propagation in the skin geometry to the skin-to-spar geometry. This phenomenon was evaluated in terms of excitability of a carrier mode in the bonded region, based on the incoming, s_0 skin mode.

The dominant displacement for s_0 is the in-plane component in the wave propagation direction, u_x, consistent with the (3,3) operation of the MFC actuator. The u_x component thus also dominates the mode conversion process at the bond edges. For the properly-cured and the poorly-cured bonds, S_0 and A_1 in Figure 3 are the carrier modes transporting the energy across the joint throughout the DC – 300 kHz frequency range examined. In fact, S_0 and A_1 are characterized by a dominant u_x displacement whose shape within the upper plate is similar to that of the incoming s_0 mode at the same frequencies. The opposite is true for either A_0 (predominant out-of-plane displacement) or SH_0 (zero in-plane displacement along the wave propagation direction). The excitation of S_0 and A_1 in the bonded region is advantageous for bond state monitoring as discussed in the previous section.

In the case of a disbonded interface, instead, it is the $S_{0,plate}$ mode in Figure 4 that transfers the energy of the incoming s_0 mode due to the similarity in cross-sectional mode shapes. This match is confirmed by the fact that the dispersion curves of $S_{0,plate}$ in Figure 4 are virtually coincident with those of s_0 (open dots) above 50 kHz. $S_{0,plate}$ remains the main energy carrier across a small disbonded region within a larger properly-bonded region, which constitutes a more realistic damage scenario. In this case, in fact, S_0 and A_1 become the incoming modes. Of the other modes potentially existing in the disbonded joint (Figure 4), some have large attenuation losses (e.g. $A_{0,plate}$), others have mode shapes too dissimilar from those of the incoming s_0, S_0 or A_1 modes (e.g. $SH_{0,spar}$, $SH_{0,plate}$, $A_{0,spar,}$ and $A_{0,plate}$), or a concentration of energy solely within the bottom spar (e.g. $S_{0,spar}$ and $A_{1,spar}$).

Making similar arguments based of the SAFE results for the [0/±45/90]s lay-up (not shown here), it can be concluded that S_0 and A_1 are the dominant carrier modes through the properly-cured and the poorly-cured joints, whereas $S_{0,plate}$ is the dominant carrier mode through the disbonded interfaces for either the [0/±45/0]s or the [0/±45/90]s lay-up.

Strength of Transmission as a Function of Bond State

The strength of transmission was estimated in the model from the cross-sectional power flow of the carrier modes, computed by the real P_x component of the Poynting vector defined by Equation (2). This quantity was divided by the normalization factor $\left(\int_H \mathbf{P}\bullet\hat{\mathbf{x}}dz\right)$, representing the power flow through the entire thickness of a unit-width waveguide and averaged over a temporal period. The normalization enabled the comparison between the various bond conditions and associated carrier modes.

Figure 5 shows the normalized P_x profiles for the $[0/\pm45/0]_S$ skin-to-spar joint for waves propagating across the bond. Notice that the discontinuities in the results for the skin layer reflect the different stiffnesses of the individual laminae in the wave propagation direction. The properly-cured bond and the poorly-cured bond are compared in the top four plots for the two carrier modes, S_0 and A_1. Figures 5(a) and 5(b) refer to S_0 propagating at 155 kHz and 205 kHz, respectively. Note that the frequency of 205 kHz is a mode coupling condition (as discussed when commenting Figure 3). This frequency is thus expected to be a "sweet spot" for large changes in transmission strength and, consequently, large sensitivity to bond state. From Figures 5(a) and 5(b), it can be seen that the strength of transmission within the upper plate will be larger in the poor bond as compared to the properly-cured bond. It is also evident in these plots that the increase in energy transmission for the poorly-cured bond will be more distinct at 205 kHz than at 155 kHz, consistently with the predicted mode coupling condition. This is a consequence of the increased through-thickness energy transfer among the bonded layers. The change in power flow between the two bond conditions is much less pronounced for the A_1 carrier mode shown in Figures 5(c) and 5(d). In fact, a slight decrease in power flow within the upper plate occurs at 205 kHz as the bond is degraded. It can be further deduced that the S_0 mode will be primarily responsible for the sensitivity to bond state based on transmission strength measurements. This conclusion is consistent with the cross-sectional strain profiles where S_0 is seen to produce larger strain than A_1 within the bond layer.

As for the disbonded case, shown in Figures 5(e) and 5(f) at 155 kHz and 205 kHz, the power flow results confirm that $S_{0,plate}$ is completely confined to the top plate. As a result, the strength of transmission should be expected to be much larger than for either one of the two carrier modes, S_0 or A_1, existing in the properly-cured and the poorly-cured conditions. The P_x power flow for the disbonded case did not change substantially over the frequency range of

interest. In fact, the result at 155 kHz in Figure 5(e) is indistinguishable from the one at 205 kHz in Figure 5(f).

The power flow results shown for the $[0/\pm45/0]_S$ plate lay-up are similar to those found for the $[0/\pm45/90]_S$ lay-up. In summary, the power flow profiles indicate that an increase in transmission strength should be expected when probing a degraded bond (whether poorly-cured or disbonded) compared to a sound, properly-cured bond.

EXPERIMENTAL TESTS ON SIMULATED WING SKIN-TO-SPAR JOINTS

Experimental Procedure

Testing was performed on the two skin-to-spar joints described in the Problem Statement. A pair of rectangular MFC transducers (dimensions of 40 mm × 25 mm × 0.3 mm) were used as wave actuator and sensor with a spacing of 115 mm as shown in Figures 1(b) and 1(c). The MFCs were bonded to the structure using a thermally-activated film adhesive. To assist in the normalization of the testing procedure, the same transducer pair was used throughout the tests. Tests run on the single skin plate confirmed that s_0 was the mode generated and detected by the MFCs with the greatest efficiency.

The signal generation and data acquisition system was a National Instruments PXI© platform running under LabVIEW that was assembled and programmed in-house. The system used an arbitrary function generator to allow for swept frequency tests using Hanning windowed tonebursts (20 V peak-to-peak) sent to the actuating MFC. The frequency sweeps were performed between 100 kHz and 300 kHz, at 1 kHz increments.

At each generation frequency, the signals detected by the MFC sensor were gated in time to isolate the predominant s_0 mode. The gated time signal was then processed through the Discrete Wavelet Transform (DWT) to extract the relevant wavelet coefficients. Greater details on the DWT processing will be given in the following section. The quantification of the ultrasonic transmission strength through the joints was achieved by taking the Root Mean Square (RMS) of both the time-domain signals and the corresponding wavelet coefficients. The RMS is related to the energy of the signal and it was computed by the well known relation:

$$\mathrm{RMS} = \sqrt{\frac{\sum_{i=1}^{Z} x_i^2}{Z}} \tag{7}$$

where x_i is a single data point within a collection of Z data points. The RMS spectra measured for the different bond conditions and plate lay-ups were then compared.

Discrete Wavelet Analysis

Extracting damage-sensitive features from the Joint Time-Frequency (JTF) domain, in addition to the conventional time domain, is becoming increasingly attractive in structural monitoring applications. Among the various JTF analyses, the DWT has been used with most success in those monitoring applications based on guided waves and requiring real-time data that are robust against noise (Staszewski, 2002; Paget et al., 2003; Rizzo and Lanza di Scalea, 2005). Briefly, the wavelet decomposition of a function $f(t)$ is calculated from the following inner product:

$$W_{\mathrm{j,n}} = \int_{-\infty}^{+\infty} f(t)\, \psi_{\mathrm{j,n}}(t)^{*}\, \mathrm{d}t \tag{8}$$

where $\psi_{\mathrm{j,n}}(t)^{*}$ is the conjugate of the mother wavelet function, $\psi_{\mathrm{j,n}}(t)$, and $W_{\mathrm{j,n}}$ are the wavelet coefficients. The parameter n (translation parameter) shifts the wavelet in time and the parameter $s = 2^{\mathrm{j}}$ (scale parameter) controls the wavelet frequency bandwidth, hence the resulting joint time-frequency analysis.

Compared to its "continuous" version that cannot be performed in real-time, the DWT is computationally efficient because of the existence of a fast orthogonal wavelet transform algorithm based on a set of filter banks (Mallat, 1999). In Mallat's filter bank tree, the DWT decomposition is done by pairs of low pass and high pass filters. Each level of decomposition, j, corresponds to a frequency band $f_{\mathrm{j}} \pm \Delta f_{\mathrm{j}}/2$. The central frequency, f_{j}, is a function of the mother wavelet central frequency, F, and the signal sampling rate, Δ, through:

$$f_{\mathrm{j}} = \frac{\Delta \times F}{2^{\mathrm{j}}} \tag{9}$$

The bandwidth, Δf_{j}, can be normally estimated as half of the distance between adjacent central frequencies. Considering Equation (9), the bandwidth can thus be written as:

$$\Delta f_{\mathrm{j}} = \left| \frac{f_{\mathrm{j+1}} - f_{\mathrm{j-1}}}{2} \right| = \frac{3}{4} f_{\mathrm{j}} \tag{10}$$

The original signal can then be reconstructed from the wavelet coefficients as follows:

$$f(t) = \sum_{j}\sum_{n} W_{j,n}\,\psi_{j,n} \tag{11}$$

The selection of a proper mother wavelet is critical for a successful application of the DWT algorithm. It can be assumed that the most effective signal decomposition is achieved by a mother wavelet with greatest similarity to the original time signal (Abbate et al., 1994). An optimization routine was adopted to identify the mother wavelet providing high correlation with the signals detected in the joint specimens. The Daubechies wavelets of orders 2, 4, 10 and 40 (db 2, db 4, db 10 and db 40) were considered in this study because their shape resembles the narrowband character of the toneburst ultrasonic signals employed. The given mother wavelet was stretched in time such that its peak frequency matched that of the time-domain signals. Zero padding was added such that the frequency resolution was equal between the stretched wavelet, $\overline{\psi_{j,n}}(t)$, and the time-domain signal, $f(t)$. Finally, the cross-correlation was computed to quantify the similarity between these two functions at each frequency value:

$$X_{corr} = \left| \overline{\psi_{j,n}}(t) \otimes f(t) \right| \tag{12}$$

The maximum cross-correlation coefficient is plotted in Figure 6 considering signals acquired across the properly-cured bond in the [0/±45/90]s joint. It can be seen that the db 10 wavelet provides the best correlation with the signals throughout the 100 kHz – 300 kHz frequency range. The low-order db 2 provides a comparable correlation only at around 200 kHz, whereas the high-order db 40 is comparable only at around 250 kHz. Hence the db 10 was chosen for the DWT decomposition of the ultrasonic signals measured in the joint specimens.

Wavelet De-noising and Compression

The DWT possesses superior de-noising and compression capabilities owing to the ability of selecting a few wavelet coefficients at given decomposition levels (pruning). Pruning, along with the ability to threshold the magnitude of the wavelet coefficients (thresholding), allows the compression of the essential signal information down to very few data points.

An example is illustrated in Figure 7, referring, again, to signals measured across the properly-cured bond of the [0/±45/90]s joint using the MFC actuator-sensor pair. Figure 7(a) shows the raw signal detected by the MFC sensor at 200 kHz, that is completely embedded into noise. The same trace, after 50 averages, is shown in Figure 7(b), where incoherent noise is reduced and the signals become clear. The early-arrival portion of the signal corresponds to

actuator-sensor cross-talk, while the late-arrival, more meaningful portion is associated with the s_0 mode. Figure 7(c) shows the DWT decomposition of the raw signal in Figure 7(a) at level 6, that was centered at 214 kHz. The result of the thresholding step is shown in Figure 7(d), where only the wavelet coefficients with amplitude above 70% of the maximum coefficient amplitude are retained and the remaining coefficients, related to noise, are discarded. By reconstructing the original signal from the thresholded, level 6 DWT coefficients of Figure 7(d), the result of Figure 7(e) is obtained. The excellent de-noising performance of this processing is clearly seen in this plot. In fact, the DWT result yields an even larger signal-to-noise ratio (SNR) than the 50-average result of Figure 7(b), without compromising the speed of the analysis. The DWT compression abilities can be seen in Figure 7(d) where as few as 5 coefficients are representative of the original, 3,000 point time-domain signal. In fact, the entire information on the s_0 mode resides exclusively in the latter two wavelet coefficients at around position 15. This level of data compression would be highly beneficial in an on-board monitoring system given the stringent requirements for data transmission and storage.

The effectiveness of the DWT can be further observed in the curves of Figure 8, representing the RMS values of the [0/±45/90]s joint signals acquired over the 100 kHz – 300 kHz range by using different numbers of averages, from 0 (raw signal) to 50. The use of a low number of averages results in an overestimation of the RMS values, although the error decays quickly once at least 5 averages are performed. Superimposed is the RMS of the reconstructed signals after DWT processing. It can be seen that the general trend of the DWT result matches very well that of the 50-average result, which should be considered the "true" solution. The difference is that the DWT processing can be done in pseudo-real time. The larger scatter in the DWT result is due to the unavoidable variability of noise content between adjacent signals. In order to cover the entire frequency range of interest, the 6^{th}, 7^{th}, and 8^{th} DWT decomposition levels were all accounted for in the reconstructions. These levels corresponded to central frequencies of 214 kHz, 107 kHz and 53.5 kHz, respectively.

Experimental Results on the Joint Specimens

The RMS spectra for the four bond states examined (properly-cured bond, poorly-cured bond, 12.7 mm × 12.7 mm disbond and 25.4 mm × 25.4 mm disbond) are summarized in Figure 9. The results are presented in terms of RMS differences from the properly-cured bond and

normalized by the same quantity. Figures 9(a) and 9(b) were obtained in the $[0/\pm45/90]_S$ lay-up from the time-domain signals and the corresponding DWT coefficients, respectively. Figures 9(c) and 9(d) were obtained in the $[0/\pm45/0]_S$ lay-up. The time-domain signals were averaged 50 times. The DWT coefficients included levels 6, 7, and 8.

The first observation from Figure 9 is that the RMS spectra obtained from the time-domain signals are extremely close to those obtained from the DWT coefficients. This, again, reaffirms the robustness of the DWT processing for extracting bond-sensitive features.

It can also be seen that all of the RMS differences are generally positive, and thus the energy transmission is strengthened in the presence of any of the bond defects considered. This general observation is consistent with the predictions made from the power flow computed using the SAFE model. The peak RMS relative change occurs between 180 kHz and 220 kHz for the $[0/\pm45/0]_S$ lay-up. This frequency range is consistent with the mode coupling conditions predicted by the model, and it is thus confirmed as the most sensitive range to detect the bond defects considered in this study. The most sensitive range is slightly shifted towards higher frequencies for the $[0/\pm45/90]_S$ lay-up, but it still partially overlaps with the predicted mode coupling conditions.

Other identifiable trends can be observed when comparing the results amongst each defect case. First, the strength of transmission of the poorly-cured bond is larger than that of the two disbonds across the entire frequency spectrum for the $[0/\pm45/0]_S$ lay-up. For the $[0/\pm45/90]_S$ lay-up, the difference between the poorly-cured bond and the large disbond is minimal. The SAFE power flow results predict that the strength of transmission should be larger for the disbond case compared to the poorly-cured bond, regardless of the skin lay-up. However, issues regarding the finite dimensions of the disbonds were not included in the model (that assumed a disbond extended for the entire width of the joint). Also, the degradation in disbond properties assumed in the model may have been too severe compared to the actual teflon inserts used in the specimens. Consequently, it can be reasonably expected that the model for the disbonded interfaces will somewhat overestimate the strength of transmission measured in the specimens.

In addition, each of the spectra in Figure 9 shows that the strength of transmission associated with the large disbond is larger than that associated to the small disbond. This trend is due to the favorable P_x component of the Poynting vector of the $S_{0,plate}$ mode (Figure 5) that isolates the

majority of the wave energy within the same skin plate where the MFC actuator and sensor are located.

Of the two specimens considered, the maximum discrimination among the different bond defects is measured in the $[0/\pm45/0]_S$ specimen seen in Figures 9(c) and 9(d).

SUMMARY AND CONCLUSIONS

The subject of this paper is the monitoring of bond state in composite-to-composite adhesive joints, specifically the wing skin-to-spar connection of UAVs. The bond monitoring approach is based on the strength of transmission of ultrasonic guided waves propagating across the bond, and generated and detected by a pair of flexible MFC transducers that lend themselves to an on-board monitoring system. Two lay-ups were investigated for the composite skin, namely a quasi-isotropic $[0/\pm45/90]_S$ lay-up and a more realistic $[0/\pm45/0]_S$ lay-up. Two types of bond defects were considered, namely a poorly-cured bond (~50% degradation in Young's modulus and shear modulus), and a disbond where the shear stiffness was nominally lost.

The wave dispersive behavior in the joints was first studied numerically by a SAFE method that accounted for viscoelastic material damping by allowing for complex stiffness matrices. Given an incoming s_0 mode, it was found by comparison of cross-sectional mode shapes that S_0 and A_1 act as the primary carrier modes through the properly-cured and the poorly-cured bonds. Since both of these modes produce increased normal and shear strains at the bondline, they are sensitive to changes in the bond stiffness. The $S_{0,plate}$ mode will, instead, act as the primary carrier mode across disbonded regions, since its energy is confined within the top skin plate. The model also indicated that frequency values between 180 kHz and 220 kHz produce mode coupling for S_0 and A_1. Mode coupling results in a large interlayer energy transfer, and it was thus expected to provide maximum sensitivity to the bond monitoring technique adopted in this study. Through the computation of the power flow (Poynting vector), the model was able to predict that the ultrasonic strength of transmission would be larger for the defected bonds compared to the properly-cured bond.

Experimental tests were conducted on two specimens constructed in the laboratory and consisting of $[0/\pm45/90]_S$ and $[0/\pm45/0]_S$ T700/5208 plates bonded to T800/924 woven tubular spars. Each joint was manufactured by creating a region of poorly-cured adhesive and two regions with isolated disbonds of two different sizes. Two MFC transducers were used as wave

actuator and sensor on either side of the bond. The strength of transmission was quantified by computing the RMS of the detected time-domain signals in the 100 kHz - 300 kHz range and the corresponding wavelet coefficients. The experimental results confirmed that the strength of transmission increases in the presence of the two types of bond defects compared to the properly-cured bond. A large sensitivity was measured corresponding to mode coupling conditions for the S_0 and A_1 carrier modes. Discrimination among the different bond defects was found maximum for the $[0/\pm45/0]_S$ lay-up. The result is encouraging, considering that the anisotropic lay-up is more representative of actual UAV wings. In both lay-ups, the measured strength of transmission generally increased with increasing disbond size.

It was demonstrated that bond-sensitive information can be extracted without compromising processing speed from selected DWT coefficients of the raw ultrasonic signals. For best performance, the DWT decomposition was performed by using a mother wavelet (db 10) that maximized the cross-correlation with the original signals in the frequency range of interest. The DWT processing is likely to become even more useful in future wave-based health monitoring systems requiring small excitation powers to the actuators and large actuator-sensor distances for increased coverage. In these cases, the SNR of the measurements can be expected to be degraded further compared to the laboratory results presented here.

Clearly, the results presented are strictly applicable to the joints examined in this study. However, the general conclusions of an increased strength of transmission in the presence of bond defects and a large sensitivity at mode coupling points, can be extended to other geometries or materials. Improvements can be made in the SAFE predictions of the power flow through the defected joints, particularly to account for disbonds of finite dimensions. Ongoing studies are aimed at making these improvements in the model, as well as examining the effects of varying temperature on the ultrasonic strength of transmission through the joints.

ACKNOWLEDGMENTS

This research was funded by the UCSD/Los Alamos Cooperative Agreement on Research and Education (CARE) and by the Los Alamos/UCSD Education Collaboration Task 2 “Structural Integrity Monitoring of UAV Composite Wings.” Thanks are extended to Prof. John Kosmatka and graduate student Jessie Oliver, Structural Engineering Department of UCSD, for fabricating the composite skin plates tested in this study.

REFERENCES

Abbate, A., Koay, J., Frankel, J., Schroeder, S.C. and P. Das. 1994. "Application of Wavelet Transform Signal Processor to Ultrasound," *Proceedings Ultrasonic Symposium,* 94CH3468-6:1147-1152

Barbezat, M., Brunner, A.J., Flüeler, P., Huber, C. and X. Kornmann. 2004. "Acoustic Emission Sensor Properties of Active Fibre Composite Elements Compared with Commercial Acoustic Emission Sensors," *Sensors and Actuators A: Physical*, 114:13-20.

Bartoli, I., Marzani, A., Lanza di Scalea, F. and E. Viola. 2005. "Modeling Wave Propagation in Damped Waveguides of Arbitrary Cross-section," *Journal of Sound and Vibration*, submitted.

Bernard, A., Lowe, M.J.S. and M. Deschamps. 2001. "Guided Waves Energy Velocity in Absorbing and Non-absorbing Plates," *Journal of the Acoustical Society of America*, 110:186-196.

Bevan, J. S. and C. Mei. 2001. "Piezoceramic Actuator Placement for Structural Acoustic and Vibration Control of Flat and Curved Panels," *Proceedings SPIE*, 4327:698-708.

Brunner, A.J., Barbezat, M., Flüeler, P. and C. Huber. 2004. "Composites from Piezoelectric Fibers as Sensors and Emitters for Acoustic Applications," *Journal of Acoustic Emission*, 22:127-137.

Chang, Z. and A.K. Mal. 1995. "A Global-local Method for Wave Propagation Across a Lap Joint," *Numerical Methods in Structural Mechanics*, 204:1-11.

Finnveden, S. 2004. "Evaluation of Modal Density and Group Velocity by a Finite Element Method," *Journal of Sound and Vibration*, 273:51-75.

Gavrić, L. 1995. "Computation of Propagative Waves in Free Rail Using a Finite Element Technique," *Journal of Sound and Vibration*, 185:531-543.

Gu, H., Lloyd, G.M. and M.L. Wang. 2005. "Interdigitated PVDF Transducers for Lamb Wave Generation and Reception," *Proceedings SPIE*, 5765: 302-312.

Hay, T.R., Wei, L., Rose, J.L. and T. Hayashi. 2003. "Rapid Inspection of Composite Skin-honeycomb Core Structures with Ultrasonic Guided Waves," *Journal of Composite Materials*, 37: 929-939.

Hayashi, T., Song, W. J. and J.L. Rose. 2003. "Guided Wave Dispersion Curves for a Bar with an Arbitrary Cross-section, a Rod and Rail Example," *Ultrasonics*, 41:175-183.

Heller, K., Jacobs, L.J. and J. Qu. 2000. "Characterization of Adhesive Bond Properties Using Lamb Waves," *NDT&E International*, 33:555-563.

Kundu, T., Maji, A., Ghosh, T. and K. Maslov. 1998. "Detection of Kissing Bonds by Lamb Waves," *Ultrasonics*, 35:573-580.

Lanza di Scalea, F., Bonomo, M. and D. Tuzzeo. 2001. "Ultrasonic Guided Wave Inspection of Bonded Lap Joints: Noncontact Method and Photoelastic Visualization," *Research in Nondestructive Evaluation*, 13:153-171.

Lanza di Scalea, F., Rizzo, P. and A. Marzani. 2004. "Propagation of Ultrasonic Guided Waves in Lap-shear Adhesive Joints: Case of Incident a0 Lamb Wave," *Journal of the Acoustical Society of America*, 115:146-156.

Lowe, M.J.S. and P. Cawley, P. 1994. "The applicability of Plate Wave Techniques for the Inspection of Adhesive and Diffusion Bonded Joints," *Journal of Nondestructive Evaluation*, 13:185-200.

Lowe, M.J.S., Challis, R.E. and C.W. Chan. 2000. "The Transmission of Lamb Waves Across Adhesively Bonded Lap Joints," *Journal of the Acoustical Society of America*, 107:1333-1345.

Mal, A.K., Chang, Z. and D. Guo. 1996. "Lap Joint Inspection Using Plate Waves," *Proceedings SPIE*, 2945:128-137.

Mal, A.K., Xu, P.C. and Y. Bar-Cohen. 1990. "Leaky Lamb Waves for the Ultrasonic Nondestructive Evaluation of Adhesive Bonds," *ASME Journal of Engineering Materials Technology*, 112:255-259.

Mallat, S.G. 1999. *A Wavelet Tour of Signal Processing*, Academic Press, New York, NY.

Monkhouse, R.S.C., Wilcox, P.D. and P. Cawley. 1997. "Flexible Interdigital PVDF Transducers for the Generation of Lamb Waves in Structures," *Ultrasonics*, 35:489-498.

Mukdadi, O.M., Desai, Y.M., Datta, S.K., Shah, A.H. and A. J. Niklasson. 2002. "Elastic Guided Waves in a Layered Plate with Rectangular Cross Section," *Journal of the Acoustical Society of America*, 112:1766-1779.

Mukdadi, O.M. and S.K. Datta. 2003. "Transient Ultrasonic Guided Waves in Layered Plates with Rectangular Cross Section," *Journal of Applied Physics*, 93:9360-9370.

Nagy, P.B. and L. Adler. 1989. "Nondestructive Evaluation of Adhesive Joints by Guided Waves," *Journal of Applied Physics*, 66:4658-4663.

Neau, G., Lowe, M.J.S. and M. Deschamps. 2002. "Propagation of Lamb Waves in Anisotropic and Absorbing Plates: Theoretical Derivation and Experiments," *Review of Progress in QNDE*, 21:1062-1068.

Paget, C.A., Grondel, S., Levin, K. and C. Delebarre. 2003. "Damage Assessment in Composites by Lamb Waves and Wavelet Coefficients," *Smart Materials and Structures*, 12:393-402.

Rizzo, P. and F. Lanza di Scalea. 2005. "Ultrasonic Inspection of Multi-wire Steel Strands with the Aid of the Wavelet Transform," *Smart Materials and Structures*, 14:1-11.

Rose, J.L., Rajana, K.M. and M.K.T. Hansch. 1995. "Ultrasonic Guided Waves for NDE of Adhesively Bonded Structures," *Journal of Adhesion*, 50:71-82.

Rose, J.L., Zhu, W. and M. Zaidi. 1998. "Ultrasonic NDT of Titanium Diffusion Bonding with Guided Waves," *Materials Evaluation*, 56:535-539.

Schoenecker, A.J., Gebhardt, S.E., Rödig, T., Keitel, U., Bruckner, B., Schnetter, J. and T. Daue. 2005. "Piezocomposite Transducers for Smart Structures Applications," *Proceedings SPIE*, 5764:34-41.

Seifried, R., Jacobs, L.J. and J. Qu. 2002. "Propagation of Guided Waves in Adhesive Bonded Components," *NDT&E International*, 35:317-328.

Staszewski, W. 2002. "Intelligent Signal Processing for Damage Detection in Composite Materials," *Composites Science and Technology*, 62:941-950.

Sun, Z., Rose, J.L. and M. Zaidi. 2002. "A Phased Array Guided Wave Approach to Adhesive Bonding Structural Integrity Analysis," *Materials Evaluation*, 61:941-946.

Thien, A.B., Chiamori, H.C., Ching, J.T., Wait, J.R. and G. Park. 2005. "Piezoelectric Active Sensing for Damage Detection in Pipeline Structures," *Proceedings 23rd International Modal Analysis Conference*, Orlando, FL, 323-336.

Wilkie, W.K., Bryant, R.G., High, J.W., Fox, R.L., Hellbaum, R.F., Jalink, A., Little, B.D. and P.H. Mirick. 2000. "Low-cost Piezocomposite Actuator for Structural Control Applications," *Proceedings SPIE's 7th Annual International Symposium on Smart Structures and Materials*, Newport Beach, CA, 323-334.

Williams, R.B. and D.J. Inman. 2002. "An Overview of Composite Actuators with Piezoceramic Fibers," *Proceedings 20th International Modal Analysis Conference*, Los Angeles, CA.

FIGURE CAPTIONS

Figure 1. (a) UAV wing skin-to-spar assembly; (b) "across the bond" test configuration; (c) and (d) test specimens with attached MFC transducers and introduced simulated damage.

Figure 2. SAFE model of wave propagation in the skin-to-spar joint: (a) modeling problem; (b) waveguide discretization with three-node, one-dimensional element.

Figure 3. Dispersion results for the $[0/\pm45/0]_S$ skin-to-spar joint (properly-cured bond) with wave propagation perpendicular to the 0-deg skin fibers: (a) phase velocity; (b) energy velocity; (c) attenuation; (d) cross-sectional strain profiles for S_0 and A_1 at 205 kHz.

Figure 4. Dispersion results for the $[0/\pm45/0]_S$ skin-to-spar joint (disbonded interface) with wave propagation perpendicular to the 0-deg skin fibers: (a) phase velocity; (b) energy velocity; (c) attenuation. Open dots show the results for the skin plate alone.

Figure 5. P_x component of the Poynting vector in the properly-cured bond and in the poorly-cured bond for (a) S_0 at 155 kHz, (b) S_0 at 205 kHz, (c) A_1 at 155 kHz, and (d) A_1 at 205 kHz. Same quantity in the disbonded case for (e) $S_{0,plate}$ at 155 kHz, and (f) $S_{0,plate}$ at 205 kHz.

Figure 6. Maximum cross-correlation coefficients between various mother wavelets and the s_0 time signal.

Figure 7. DWT processing: (a) MFC raw signal at 200 kHz; (b) MFC signal after 50 averages; (c) wavelet coefficients of raw signal at decomposition level 6; (d) 70% thresholded wavelet coefficients of raw signal at decomposition level 6; (e) reconstructed signal from wavelet coefficients in (d).

Figure 8. Root mean square of s_0 time signals after performing various numbers of averages and after performing DWT analysis of the raw signals.

Figure 9. Normalized root mean square differences of the defected bonds relative to the properly-cured bond: (a) time-domain signals for the $[0/\pm45/90]_S$ joint; (b) DWT-processed signals for the $[0/\pm45/90]_S$ joint; (c) same as (a) for the $[0/\pm45/0]_S$ joint; (d) same as (b) for the $[0/\pm45/0]_S$ joint.

TABLE CAPTIONS

Table 1. Real and imaginary stiffness coefficients, geometric and physical properties for the bonded layers.

Table 2. Ultrasonic bulk longitudinal and shear velocities and material attenuations for the adhesive layer.

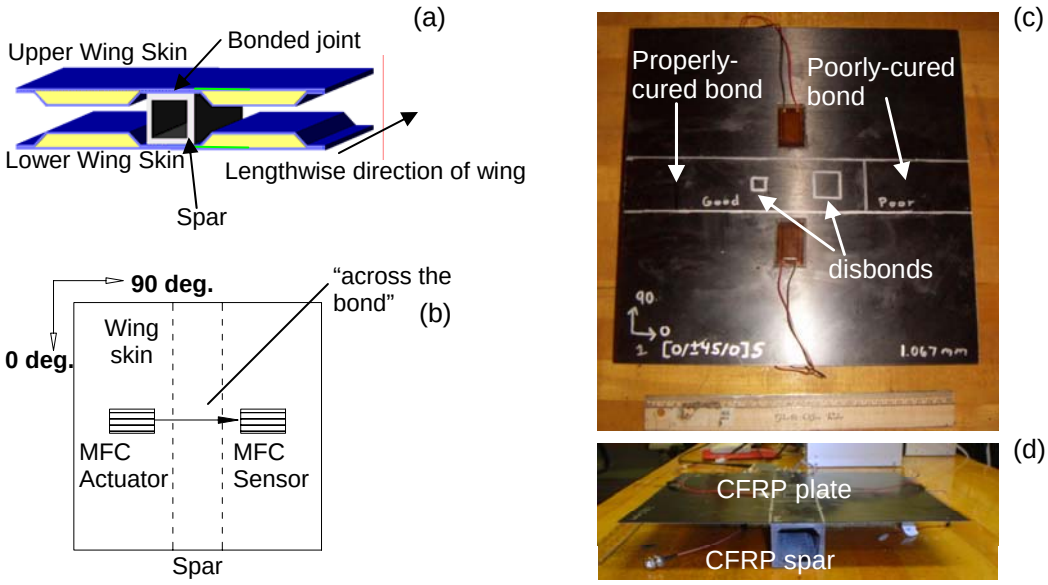

Figure 1. (a) UAV wing skin-to-spar assembly; (b) "across the bond" test configuration; (c) and (d) test specimens with attached MFC transducers and introduced simulated damage.

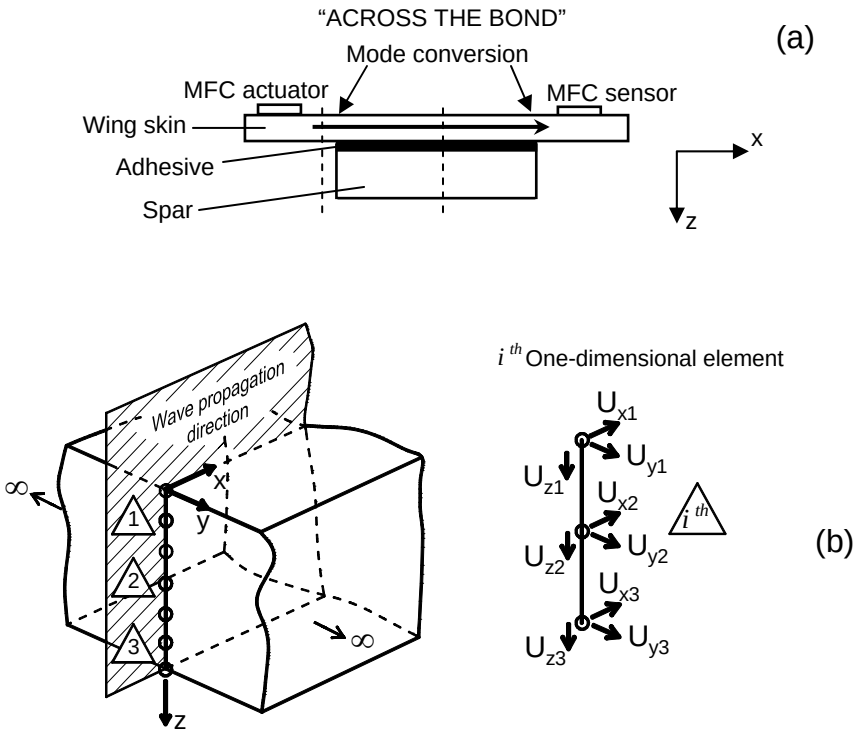

Figure 2. SAFE model of wave propagation in the skin-to-spar joint: (a) modeling problem; (b) waveguide discretization with three-node, one-dimensional element.

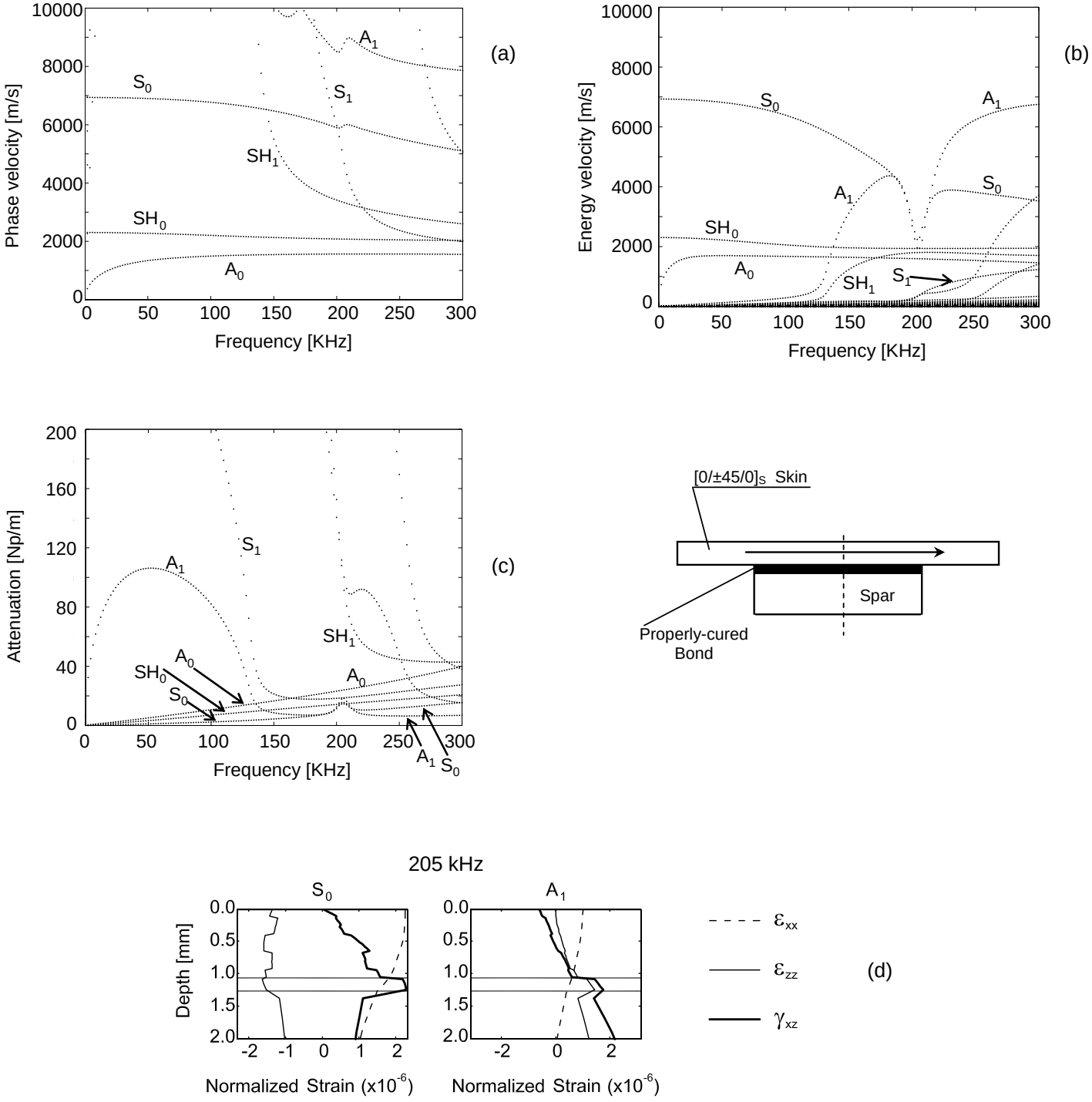

Figure 3. Dispersion results for the $[0/\pm45/0]_S$ skin-to-spar joint (properly-cured bond) with wave propagation perpendicular to the 0-deg fibers: (a) phase velocity; (b) energy velocity; (c) attenuation; (d) cross-sectional strain profiles for S_0 and A_1 at 205 kHz.

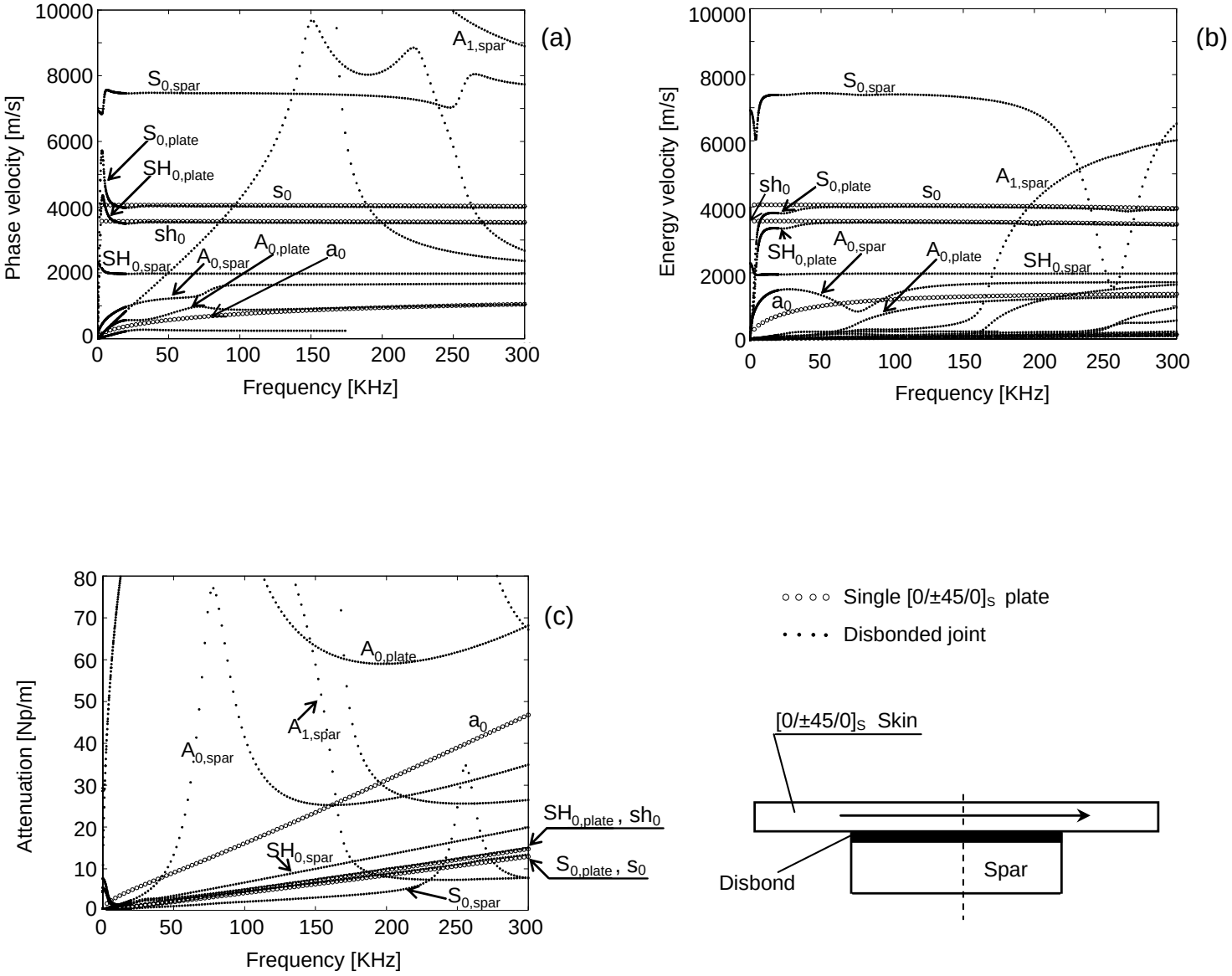

Figure 4. Dispersion results for the $[0/\pm45/0]_S$ skin-to-spar joint (disbonded interface) with wave propagation perpendicular to the 0-deg skin fibers: (a) phase velocity; (b) energy velocity; (c) attenuation. Open dots show the results for the skin plate alone.

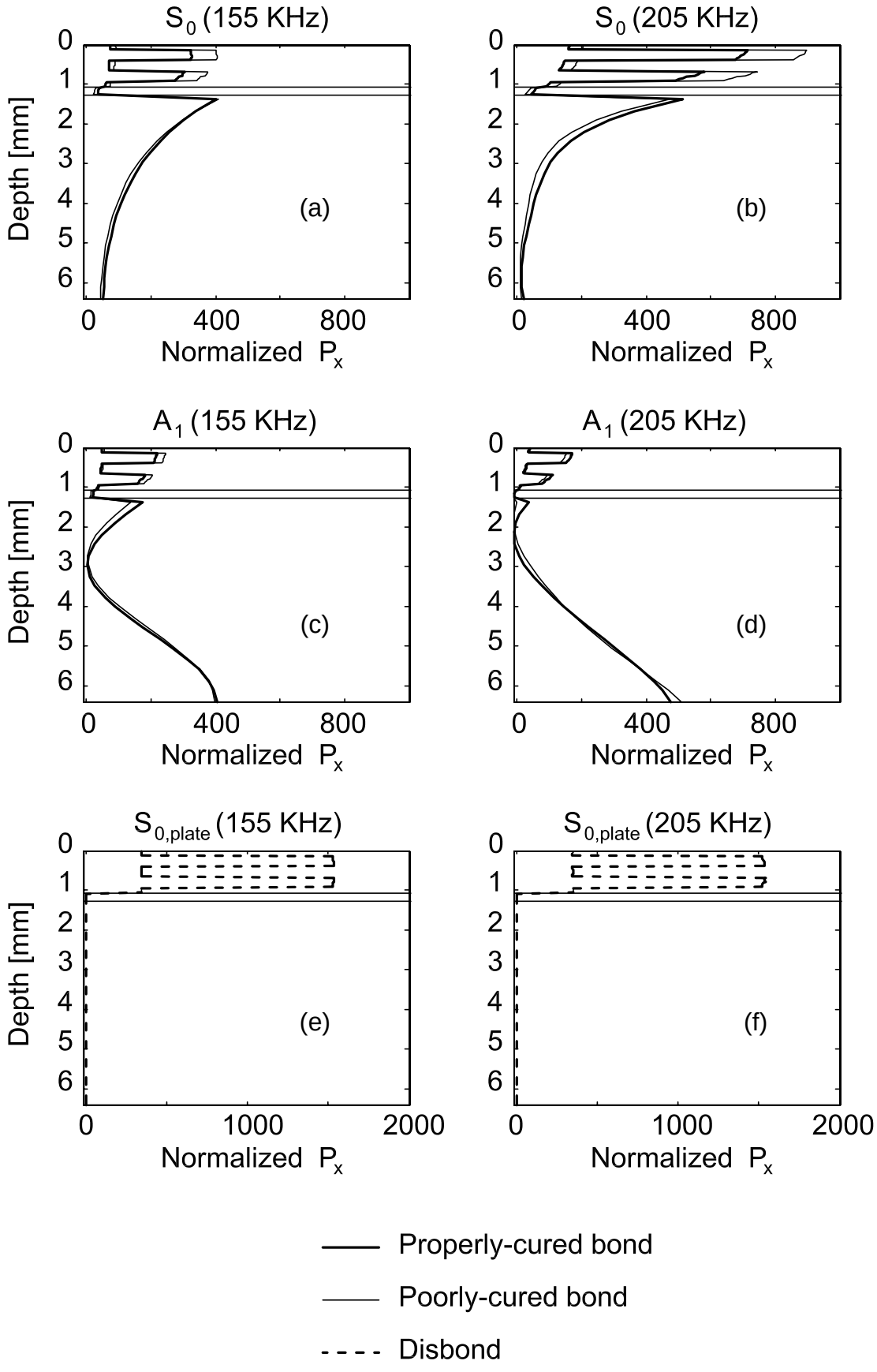

Figure 5. P_x component of the Poynting vector in the properly-cured bond and in the poorly-cured bond for (a) S_0 at 155 kHz, (b) S_0 at 205 kHz, (c) A_1 at 155 kHz, and (d) A_1 at 205 kHz. Same quantity in the disbonded case for (e) $S_{0,plate}$ at 155 kHz, and (f) $S_{0,plate}$ at 205 kHz.

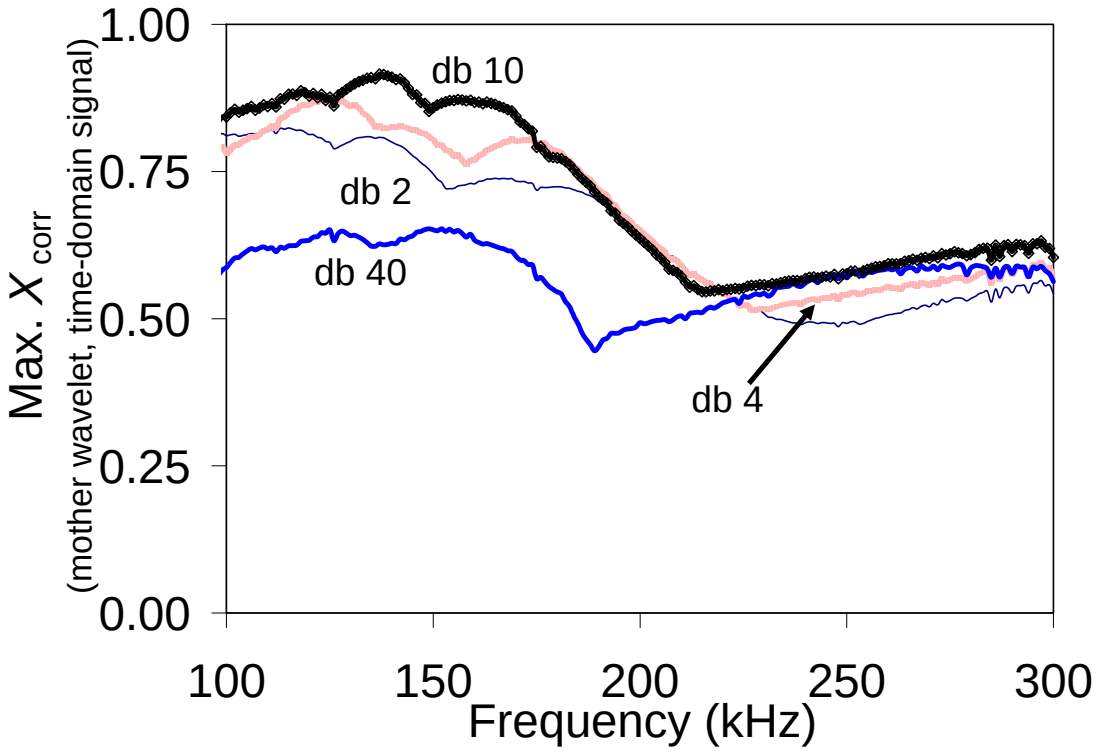

Figure 6. Maximum cross-correlation coefficients between various mother wavelets and the s_0 time signal.

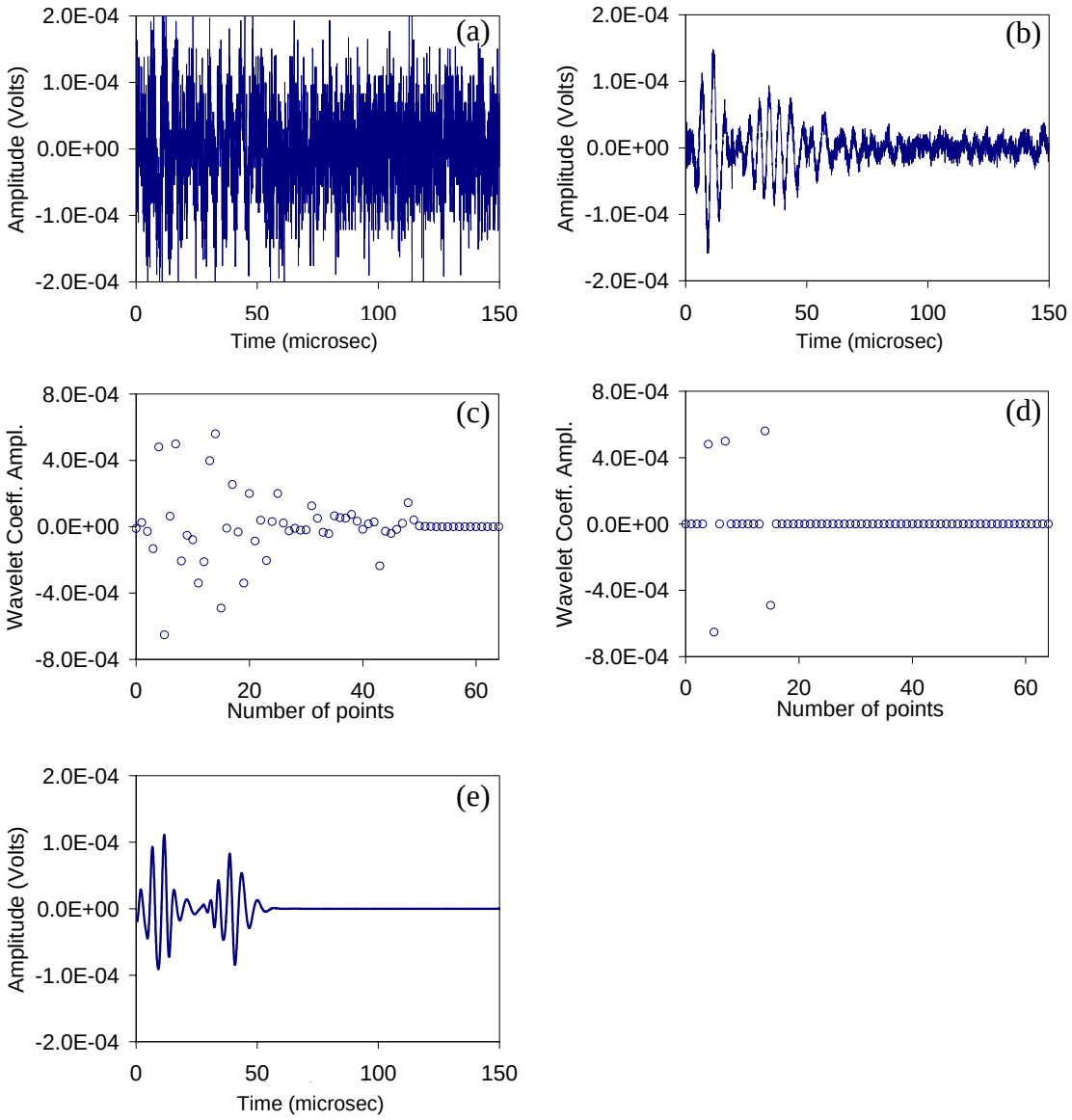

Figure 7. DWT processing: (a) MFC raw signal at 200 kHz; (b) MFC signal after 50 averages; (c) wavelet coefficients of raw signal at decomposition level 6; (d) 70% thresholded wavelet coefficients of raw signal at decomposition level 6; (e) reconstructed signal from wavelet coefficients in (d).

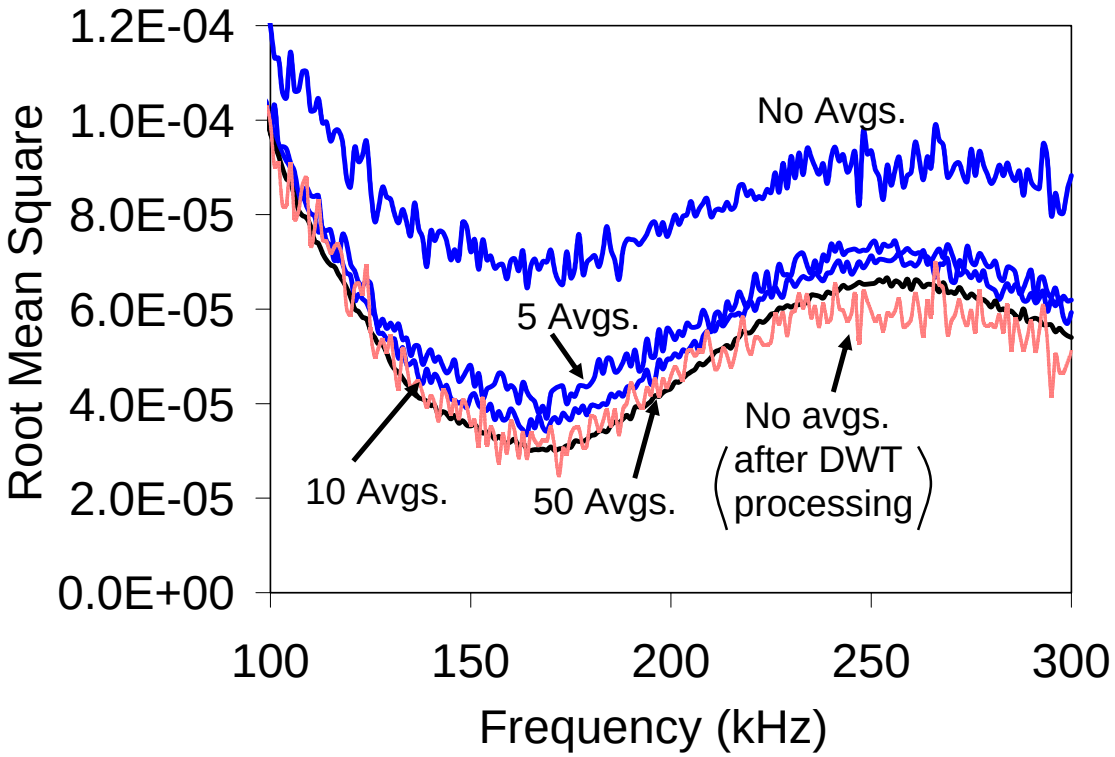

Figure 8. Root mean square of s_0 time signals after performing various numbers of averages and after performing DWT analysis of the raw signals.

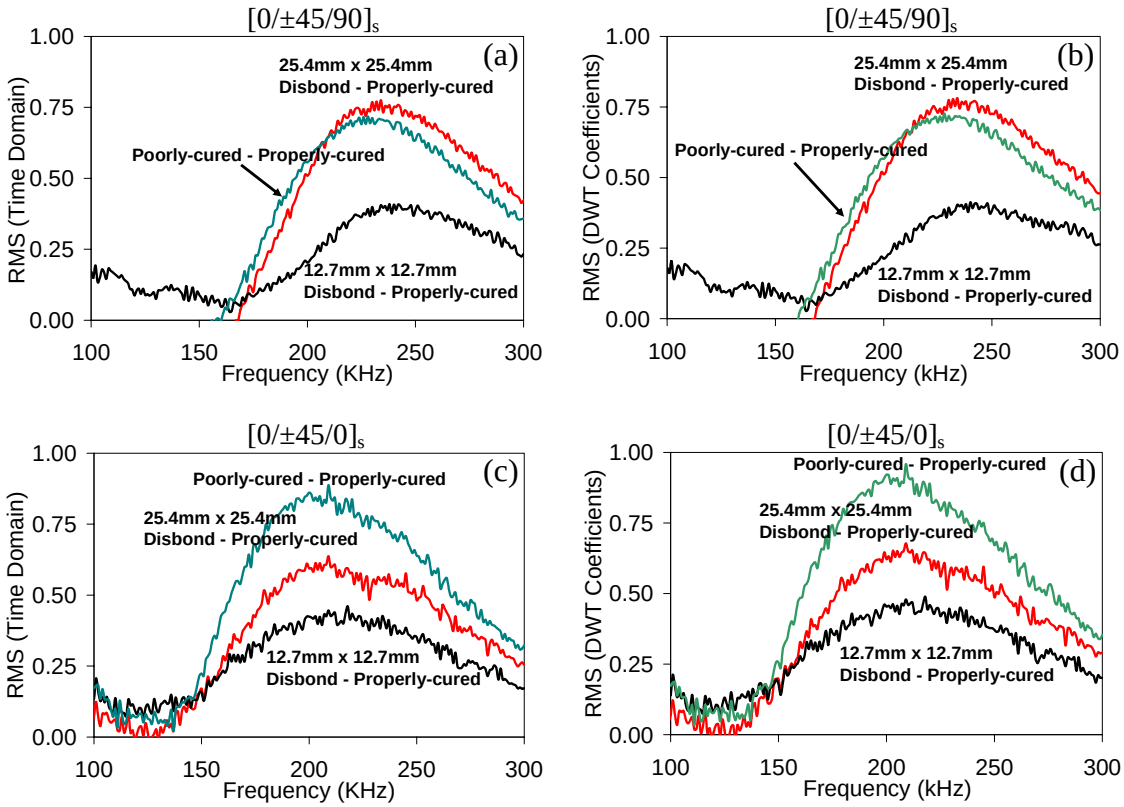

Figure 9. Normalized root mean square differences of the defected bonds relative to the properly-cured bond: (a) time-domain signals for the $[0/\pm45/90]_S$ joint; (b) DWT-processed signals for the $[0/\pm45/90]_S$ joint; (c) same as (a) for the $[0/\pm45/0]_S$ joint; (d) same as (b) for the $[0/\pm45/0]_S$ joint.

Table 1. Real and imaginary stiffness coefficients, geometric and physical properties for the bonded layers.

Layer	C'_{11} [GPa] (C''_{11}) [GPa]	C'_{12} [GPa] (C''_{12}) [GPa]	C'_{13} [GPa] (C''_{13}) [GPa]	C'_{22} [GPa] (C''_{22}) [GPa]	C'_{23} [GPa] (C''_{23}) [GPa]	C'_{33} [GPa] (C''_{33}) [GPa]	C'_{44} [GPa] (C''_{44}) [GPa]	C'_{55} [GPa] (C''_{55}) [GPa]	C'_{66} [GPa] (C''_{66}) [GPa]	Density [kg/m^3]	Thickness [mm]
CFRP Lamina	135 (8.23)*	5.70 (0.65)*	5.70 (0.60)*	14.2 (0.34)*	8.51 (0.25)*	14.2 (0.65)*	2.87 (0.24)*	4.55 (0.28)*	4.55 (0.25)*	1530	0.133
CFRP Spar	88.0 (4.28)	5.45 (0.65)	5.09 (0.425)	88.0 (4.28)	5.09 (0.425)	11.3 (0.65)	4.64 (0.26)	4.64 (0.26)	6.00 (0.25)	1530	5.235
Properly-cured Bond	8.24 (0.39)	4.10 (0.028)	4.10 (0.028)	8.24 (0.39)	4.10 (0.028)	8.24 (0.39)	2.07 (0.18)	2.07 (0.18)	2.07 (0.18)	1421	0.203
Poorly-cured Bond	6.89 (0.19)	4.58 (0.064)	4.58 (0.064)	6.89 (0.19)	4.58 (0.064)	6.89 (0.19)	1.16 (0.066)	1.16 (0.066)	1.16 (0.066)	1465	0.203
Disbond	0.0697 (0.0352)	0.0695 (0.0349)	0.0695 (0.0349)	0.0697 (0.0352)	0.0695 (0.0349)	0.0697 (0.0352)	0.000118 (0.000128)	0.000118 (0.000128)	0.000118 (0.000128)	1421	0.203

* From Neau et al., 2002

Table 2. Ultrasonic bulk longitudinal and shear velocities and material attenuations for the adhesive layer.

Layer	C_L [m/s]	C_T [m/s]	α_L [Np/λ]	α_T [Np/λ]
Properly-cured Bond	2410	1210	0.149	0.276
Poorly-cured Bond	2170	890	0.089	0.178
Disbond	241	12.1	1.497	2.763